

Embedded AGN and star formation in the central 80 pc of IC 3639[★]

J. A. Fernández-Ontiveros^{1,2,3}, K. R. W. Tristram⁴, S. Hönig⁵, P. Gandhi⁵, and G. Weigelt³

¹ Instituto de Astrofísica de Canarias (IAC), C/Vía Láctea s/n, E-38205 La Laguna, Tenerife, Spain
e-mail: j.a.fernandez.ontiveros@gmail.com, jafo@iac.es

² Universidad de La Laguna (ULL), Dpto. Astrofísica, Avd. Astrofísico Fco. Sánchez s/n, E-38206 La Laguna, Tenerife, Spain

³ Max-Planck-Institut für Radioastronomie (MPIfR), Auf dem Hügel 69, D-53121 Bonn, Germany

⁴ European Southern Observatory, Alonso de Córdova 3107, Vitacura, Santiago, Chile

⁵ School of Physics & Astronomy, University of Southampton, Southampton SO17 1BJ, UK

September 24, 2018

ABSTRACT

Aims. Our goal is to probe the inner structure and the nature of the mid-IR emission in the active galaxy IC 3639, which hosts a Seyfert 2 nucleus and shows signatures of strong star-forming activity.

Methods. We use interferometric observations in the *N*-band with VLTI/MIDI to resolve the mid-IR emission of this nucleus. The origin of the nuclear infrared emission is determined from: 1) the comparison of the correlated fluxes from VLTI/MIDI with the fluxes measured at subarcsec resolution (VLT/VISIR, VLT/ISAAC); 2) diagnostics based on IR fine-structure line ratios, the IR continuum emission, IR bands produced by polycyclic aromatic hydrocarbons (PAH) and silicates; and 3) the high-angular resolution spectral energy distribution.

Results. A large fraction of the total mid-IR emission of IC 3639 is produced in the innermost $\lesssim 80$ pc with only $\sim 1\%$ of the total luminosity released in the UV/optical range. The unresolved flux of IC 3639 is 90 ± 20 mJy at $10.5 \mu\text{m}$, measured with three different baselines in VLTI (UT1–UT2, UT3–UT4, and UT2–UT3; 46–58 m), making this the faintest measurement so far achieved with mid-IR interferometry. The correlated flux is a factor of 3–4 times fainter than the VLT/VISIR total flux measurement. The observations suggest that most of the mid-IR emission has its origin on spatial scales between 10 and 80 pc (40–340 mas). The emission confined within the inner 80 pc is either dominated by a starburst component or by the AGN core. The brightness distribution could be reproduced by a single component associated to the AGN, although this scenario would imply a very extended dust distribution when compared to other nearby Seyfert galaxies detected with MIDI. The extended component could also be associated to polar dust emission, i.e. a dusty wind blown by the AGN. However, a mixed contribution dominated by the star formation component over the AGN is favoured by the diagnostics based on ratios of IR fine-structure emission lines, the shape of the IR continuum, and the PAH and silicate bands.

Conclusions. A composite AGN-starburst scenario is able to explain both the mid-IR brightness distribution and the IR spectral properties observed in the nucleus of IC 3639. The nuclear starburst would dominate the mid-IR emission and the ionisation of low-excitation lines (e.g. $[\text{Ne II}]_{12.8\mu\text{m}}$) with a net contribution of $\sim 70\%$. The AGN accounts for the remaining $\sim 30\%$ of the mid-IR flux, ascribed to the unresolved component in the MIDI observations, and the ionisation of high-excitation lines (e.g. $[\text{Ne V}]_{14.3\mu\text{m}}$ and $[\text{O IV}]_{25.9\mu\text{m}}$).

Key words. galaxies: Seyfert – galaxies: starburst – infrared: galaxies – techniques: interferometric

1. Introduction

The central regions of nearby galaxies are excellent laboratories to probe the connection between Active Galactic Nuclei (AGN) and starburst activity. The $M-\sigma$ relation suggests a coupling between both phenomena, since the growth of the black hole (BH) correlates with the properties of the stellar bulge (Kormendy & Richstone 1995; Gebhardt et al. 2000). This coexistence has been identified up to $z \sim 2$, where strong AGN activity co-evolve with star formation in galaxies, both embedded in a dust enshrouded phase mostly obscured to optical wavelengths, but revealed in the infrared (IR) range (Madau & Dickinson 2014). The main uncertainties arise when we try to address the interplay and evolution of AGN and star formation, for instance if gas heating and outflows from the AGN quench the star-formation process and further AGN activity, self-regulating the growth of the BH (Springel & Hernquist 2003; Di Matteo et al. 2005; Ciotti

& Ostriker 2007). Alternatively, there might be a triggering of the AGN activity produced by the starburst itself, driving the material into the innermost parsecs to fuel the supermassive BH (Kawakatu & Wada 2008; Wutschik et al. 2013).

Although AGN and starburst activity show coexistence in time, with short delays between them (~ 100 – 200 Myr, Davies et al. 2007; Wild et al. 2010), they are typically identified at very different spatial scales. While the AGN releases its energy within a region of a few Schwarzschild radii, nuclear star-forming regions have been spatially resolved from ~ 100 pc to kiloparsec-size rings (González Delgado et al. 1998; Wilson et al. 2000; Knapen 2005). Traces of star-formation have also been detected in the inner few tens of parsecs of AGN, possibly associated with the torus (e.g. Davies et al. 2007; Esquej et al. 2014). Such a mechanism is sometimes invoked in torus models in order to support its vertical structure, for example, through supernovae (SNe) explosions (Wada & Norman 2002; Vollmer et al. 2008, Schartmann et al. 2009). On the other hand, interferometric observations in the IR of nearby AGN have changed our picture

[★] Based on observations collected at the European Southern Observatory, Chile, programmes 070.B-0393, 088.D-0005 and 088.B-0809.

Table 1. Optical, IR photometry, and IR emission lines and spectral features measured for the nucleus of IC 3639. Optical photometric fluxes have been corrected by Galactic extinction ($E(B - V) = 0.06$ mag; Schlafly & Finkbeiner 2011; Cardelli et al. 1989). In the subsequent analysis, data were also corrected for redshift.

Instrument/Filter	λ (μm)	$\Delta\lambda$ (μm)	Flux (mJy)	Aperture
FOC/F210M	0.22	0.04	$(17 \pm 2) \times 10^{-3}$	0'14
WFPC2/F606W	0.60	0.15	0.22 ± 0.02	0'14
ISAAC/L-band	3.78	0.58	18.9 ± 0.2	0'50
ISAAC/M-band	4.66	0.10	32 ± 1	0'50
T-ReCS/N-band	10.36	2.64	305 ± 9^a	0'40
VISIR/PAH2	11.25	0.59	326 ± 17^b	0'40
VISIR/NEII	12.81	0.10	532 ± 30	0'50
VISIR/NEII_2	13.04	0.22	543 ± 29^b	0'40
MIDI/N-band (UT2–UT3)	10.5	2.5	84 ± 17^c	0'52
MIDI/N-band (UT1–UT2)	10.5	2.5	95 ± 21^c	0'52
MIDI/N-band (UT3–UT4)	10.5	2.5	90 ± 17^c	0'52

Instrument	Line	Flux ($\times 10^{-17}$ W m $^{-2}$)	Slit width
ESO-MPG2.2m/EFOSC2	[O III] $_{5007\text{\AA}}^{\text{obs}}$	20.3 ± 0.2^d	$\sim 1''$
ESO-MPG2.2m/EFOSC2	[O III] $_{5007\text{\AA}}^{\text{cor}}$	185.7 ± 1.8^d	$\sim 1''$
Spitzer/IRS	PAH $_{11.3\mu\text{m}}$	111^e	$4'7 \times 11'3$
Spitzer/IRS	[Ne II] $_{12.8\mu\text{m}}$	45.2 ± 0.5^e	$4'7 \times 11'3$
Spitzer/IRS	[Ne V] $_{14.3\mu\text{m}}$	11.2 ± 0.6^e	$4'7 \times 11'3$
Spitzer/IRS	[Ne III] $_{15.6\mu\text{m}}$	27.0 ± 0.4^e	$4'7 \times 11'3$
Spitzer/IRS	[O IV] $_{25.9\mu\text{m}}$	21.2 ± 0.6^e	$11'1 \times 22'3$
Herschel/PACS	[O III] $_{88\mu\text{m}}$	41.9 ± 1.7^f	$28'2 \times 28'2$
VISIR	[S IV] $_{10.5\mu\text{m}}$	7.1 ± 1.6	0'52
VISIR	PAH $_{11.3\mu\text{m}}$	41.4 ± 0.4	0'52
VISIR	[Ne II] $_{12.8\mu\text{m}}$	33.4 ± 1.0	0'52

Notes. ^(a) PSF photometry from Asmus et al. (2014). ^(b) Photometry from Gandhi et al. (2009). ^(c) Correlated flux in the UT2–UT3 (46 m), UT1–UT2 (56.5 m), and UT3–UT4 (57.8 m) baselines. ^(d) Line fluxes from Temporin et al. (2003), including both observed and corrected fluxes from the measured Balmer decrement of 6.1, assuming an intrinsic decrement of 3.0 (Bassani et al. 1999). ^(e) Line fluxes from Tommasin et al. (2008). ^(f) Line flux from Fernández-Ontiveros et al. (2016).

of the dusty media surrounding the central engine (the torus; e.g. Weigelt et al. 2004, Jaffe et al. 2004, Bartscher et al. 2013, Hönig et al. 2013, Tristram et al. 2014, López-Gonzaga et al. 2014), and also the cold molecular gas revealed by ALMA (García-Burillo et al. 2016, Gallimore et al. 2016, Aalto et al. 2017). A theoretical scenario to describe the observed characteristics has been proposed recently by Hönig & Kishimoto (2017), including an extended dusty wind dominating the mid-IR flux and a compact geometrically-thin disc component dominating the near-IR bump. However, it is not clear what is the effect of star formation happening in the innermost few parsecs of a galaxy, which mechanisms can regulate the interplay with the central BH, and what is the impact on the obscuration and the dust distribution in the torus.

IC 3639 is a source well suited to explore the AGN-starburst connection. This Seyfert 2 nucleus shows mixed characteristics with star formation activity (González Delgado et al. 1998), a relatively bright mid-IR core (~ 320 mJy; Asmus et al. 2014), and a broad H α component in polarised light suggesting the presence of a hidden type 1 nucleus (Heisler et al. 1997; Lumsden et al. 2001). Its nucleus is strongly absorbed in X-rays ($N_H > 3.6 \times 10^{24}$ cm $^{-2}$, i.e. Compton-thick; Boorman et al. 2016). In the UV, images from the Faint Object Camera (FOC) on board the *Hubble Space Telescope* (HST) reveal an extended morphology along the east-west axis (González Delgado et al. 1998; see Fig. 1, right panel). Three main regions are resolved by HST/FOC: a fainter compact one – assumed to be the nucleus – located in the centre, which is surrounded by two brighter and

extended lobes at a distance of $\sim 0'2$ (48 pc; $D = 49.4$ Mpc from NED¹). Still, it is not clear whether these lobes correspond to circumnuclear star-formation (González Delgado et al. 1998) or to the narrow-line region (NLR; Ghosh et al. 2007). Furthermore, a kinematic study in the UV performed by Fischer et al. (2013) to determine the NLR orientation was not conclusive for the IC 3639. Finally, an extended radio jet has not been reported in the literature for this object, although extended radio emission at subarcsec scales was found by Thean et al. (2000).

Due to the compactness of the emission in the mid-IR, the nucleus of IC 3639 is an obvious target for the MID-infrared Interferometric instrument (MIDI) at the Very Large Telescope Interferometer (VLTI). In the *N*-band, this source is unresolved at 0'4 resolution in VLT/VISIR² images (see Fig. 1 right panel UV–IR comparison; also Asmus et al. 2014). The point-like emission is ascribed to the UV and optical central peak, but no counterpart has been found in the mid-IR down to ~ 15 mJy for the two bright UV peaks surrounding the nucleus (Gandhi et al. 2009; Asmus et al. 2014). With a mid-IR flux of ~ 320 mJy, IC 3639 was one of the targets included in the MIDI AGN Large program³, a campaign performed with VLTI/MIDI. However, no interferometric signal could be detected for the nucleus of IC 3639. A flux limit of $F_\nu < 150$ mJy was derived for this target for a projected baseline length of 56 m using the UT1–UT2 con-

¹ $H_0 = 73$ km s $^{-1}$ Mpc $^{-1}$, $\Omega_m = 0.27$, $\Omega_\Lambda = 0.73$.

² VLT Imager and Spectrometer for mid-Infrared (Lagage et al. 2004).

³ ESO program number 184.B-0832.

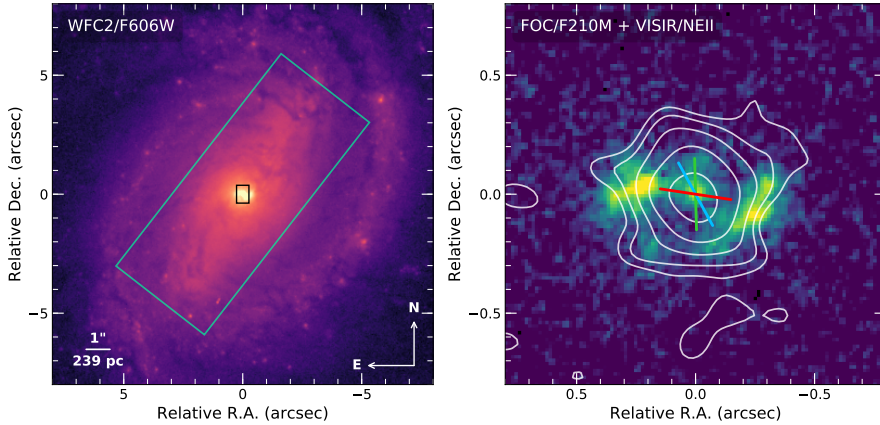


Fig. 1. *Left:* *HST*/WFC2 image of IC 3639 acquired with the filter F606W. The black rectangle represents the size of the slit used to extract the VISIR spectrum ($0''.75 \times 0''.52$), while the green square corresponds to the slit size and orientation of the *Spitzer*/IRS-SH observations ($9.9\text{--}19.5\ \mu\text{m}$, $4''.7 \times 11''.3$). *Right:* *HST*/FOC image acquired with the filter F210M from González Delgado et al. (1998). The white contours correspond to the VISIR/SPEC NEII filter image. The orientation of the different baselines used for MIDI observations are indicated by the blue (UT2–UT3), green (UT1–UT2), and red (UT3–UT4) lines.

figuration (Burtscher et al. 2013). This motivated our targeted observation of this source using the experimental VLT/MIDI “no-track” mode, which allows the detection of faint sources where fringes cannot be tracked.

The observations and the data reduction are explained in Section 2, the main results are presented in Section 3, and its main implications for the AGN-starburst connection are discussed in Section 4. Finally, in Section 5 we summarise the main conclusions from this study.

2. Dataset

The new observations in the mid-IR were carried out with VLT/MIDI and VLT/VISIR. These were complemented with archival mid-IR spectra from the Infrared Spectrograph on board *Spitzer*, *L* and *M*-band images from VLT/ISAAC and *HST* optical and UV images. Flux measurements of the AGN derived from these data, corrected for Galactic reddening, are included in Table 1.

2.1. Mid-IR observations

IC 3639 was observed with MIDI (Leinert et al. 2003), a Michelson dual-beam combiner for spectro-interferometric observations in the $8\text{--}13\ \mu\text{m}$ wavelength range, located at the Very Large Telescope Interferometer (VLT), Cerro Paranal, Chile. Very faint fringes on IC 3639 were detected under very stable atmospheric conditions on the nights of February 5th (UT1–UT2 configuration), and February 10th 2012 (UT3–UT4 and UT2–UT3). The projected baselines are $56.5\ \text{m}$ ($PA = 1.5^\circ$), $57.8\ \text{m}$ (81.4°), and $46.0\ \text{m}$ (28.6°), respectively. The faintness of this target in the *N*-band prevents the use of the standard fringe tracking mode. Thus, the observations were performed using the no-tracking mode, i.e. the fringes were scanned blindly – with the group-delay tracking switched off – close to the zero optical path delay, derived for the calibrator (HD 108759). During the first night (UT1–UT2), a brighter AGN – IC 4329A – was observed close in time with the same instrumental configuration. The spectral properties of IC 4329A are similar to those of IC 3639 and hence allow us to robustly constrain the correlated flux of IC 3639. For the second night (UT3–UT4 and UT2–UT3), the correlated flux was determined with the help of another bright target, V838 Mon⁴.

⁴ This source was originally observed for a different science case under programme 088.D–0005.

The data of IC 3639 is too faint to be processed by the standard MIDI data reduction software *MIA+EWS* (Jaffe 2004). Instead, we developed further the method presented in Burtscher et al. (2012) in order to estimate the correlated flux of a faint source. To obtain an estimate of the broadband correlated flux from the resulting data, the signal of IC 3639 was compared to that of the brighter sources, IC 4329A and V838 Mon. The latter were reduced by a certain factor and mixed with the noise recorded in IC 3639 to mimic its signal. We found that the correlated flux of IC 4329A ($F_\nu \sim 700\ \text{mJy}$) needs to be reduced by a factor of $\sim 0.13 \pm 0.03$ to match the signal observed for IC 3639, implying a correlated flux of $95 \pm 21\ \text{mJy}$ for IC 3639 on the UT1–UT2 baseline. V838 Mon ($F_\nu \sim 800\ \text{mJy}$) required a reduction by a factor of ~ 0.11 (UT3–UT4) and 0.10 (UT2–UT3), corresponding to correlated fluxes of $90 \pm 17\ \text{mJy}$ and $84 \pm 17\ \text{mJy}$, respectively. With this method only an estimate of the broadband correlated flux can be obtained, the spectral information cannot be recovered.

In parallel, low-resolution ($R \sim 350$) mid-IR spectra were acquired with VLT/VISIR on February 5th, 2012 (8.5 and $9.8\ \mu\text{m}$ spectral settings; calibrator HD 102964) and March 8th 2012 (11.4 and $12.4\ \mu\text{m}$ spectral settings; calibrator HD 168592). The data were reduced and calibrated using the ESO Common Pipeline Library (CPL v5.3.1, VISIR recipe v3.4.4), and post-processed using the methods described in Hönig et al. (2010). The final spectrum was extracted from a $0''.75 \times 0''.52$ slit, which mimics the slit characteristics of MIDI (slit represented as a black rectangle in Fig. 1, left panel; the spectrum is shown in red colour in Fig. 2). Additionally, aperture photometry ($0''.5$ radius, background estimated in a $0''.6\text{--}0''.8$ annulus) of the science target was performed on the NEII filter acquisition image, taken simultaneously with the spectra ($\lambda = 12.81\ \mu\text{m}$, $\Delta\lambda = 0.21\ \mu\text{m}$; calibrator HD 168592).

The continuum fluxes measured in the VISIR images are listed in Table 1. The latter also includes the integrated fluxes measured in the VISIR spectrum for the $[\text{Si IV}]_{10.5\ \mu\text{m}}$ and $[\text{Ne II}]_{12.8\ \mu\text{m}}$ emission lines, and the $\text{PAH}_{11.3\ \mu\text{m}}$ feature. In all cases, the continuum contribution has been subtracted using a linear interpolation to the continuum adjacent to the corresponding emission line or feature.

2.2. Archival data

In our analysis we included a mid-IR spectrum acquired with the InfraRed Spectrograph (IRS) on board the *Spitzer Space Tele-*

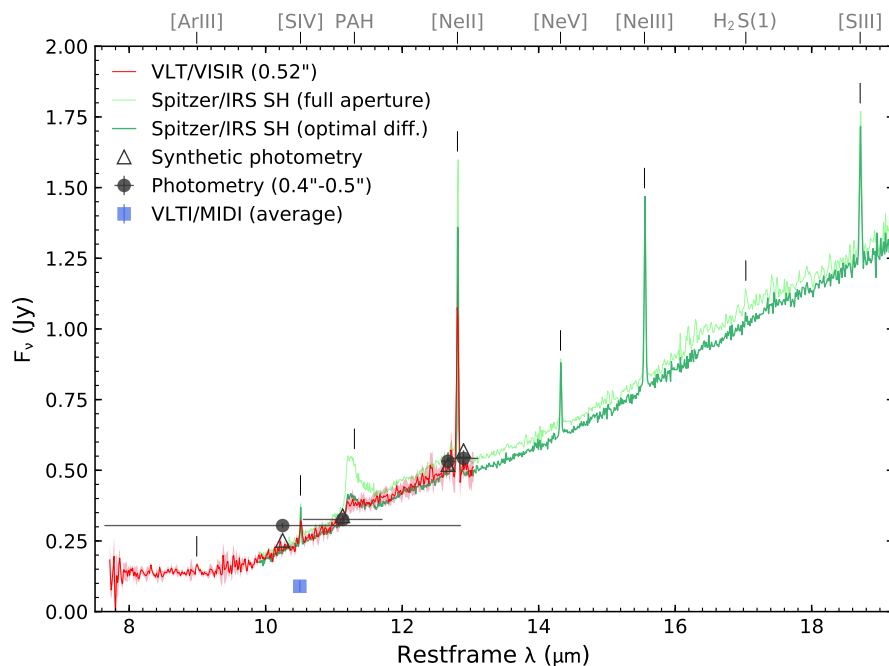


Fig. 2. Mid-IR rest-frame spectrum of IC 3639. In red, the VLT/VISIR spectrum acquired with a slit size of $0''.75 \times 0''.52$ and a spectral resolution of $R \sim 350$. In light green, the *Spitzer*/IRS spectrum at $R \sim 600$ obtained from the full-aperture extraction (slit size of $4''.7 \times 11''.3$). In dark green, the optimal-difference extracted spectrum of the same observation (see text). Both IRS spectra were taken from the CASSIS atlas (Lebouteiller et al. 2015). Black circles correspond to VLT/VISIR photometric measurements at $\sim 0''.5$ resolution (96 pc). The average correlated flux estimated from VLT/MIDI (~ 90 mJy), is represented by the blue square. Black open triangles correspond to synthetic photometry performed on the VISIR spectrum. Note that no scaling has been applied to the *Spitzer*/IRS-SH spectrum, thus the match between the continuum level in both spectra suggests that the point-like source seen by VISIR dominates also the *Spitzer*/IRS-SH spectrum. Emission lines stand out in the IRS spectrum due to the higher spectral resolution.

scope (PI: G. Fazio; AOR key: 17961984; see Fig. 2), using the high-spectral resolution mode ($R \sim 600$). The latter covers the 9.9–37.1 μm range with slit sizes of $4''.7 \times 11''.3$ (SH mode: 9.9–19.5 μm ; green slit in Fig. 1) and $11''.1 \times 22''.3$ (LH mode: 18.8–37.1 μm). Two different extractions of the same spectrum were taken from the Cornell Atlas of *Spitzer*/Infrared Spectrograph Sources (CASSIS; Lebouteiller et al. 2015): the full-aperture extraction (light green spectrum in Fig. 2), and the optimal-differential extraction (dark green spectrum in Fig. 2). The former is obtained from the collapse of the 2D spectrum along the wavelength axis within the full-aperture slit ($4''.7 \times 11''.3$ for the SH range). In the optimal-differential method, the pipeline used in CASSIS takes advantage of the PSF profile and the two nod images to improve the S/N ratio and produce a background-subtracted spectrum (see Lebouteiller et al. 2015). This method is particularly suited for unresolved sources mixed with extended emission. Note that no offset scaling has been applied to the *Spitzer*/IRS spectra, whose continuum level matches perfectly the VISIR spectrum in the 10–13 μm range. Line fluxes measured by Tommasin et al. (2008) in a full-aperture extraction of the *Spitzer*/IRS high-spectral resolution (HR) spectrum are listed in Table 1.

VLT/ISAAC *L* and *M*-band observations were taken from the ESO scientific archive (July 15th 2003, programme 070.B-0393) and are included in Table 1. The data reduction was performed using the *jitter* task within ECLIPSE (Devillard 1999), including background subtraction, registration, and combination of individual frames. Flux calibration was based in the near-IR standard HD 106965 (UKIRT standards; Leggett et al. 2003). The photometry in the *L* and *M*-band images was extracted using a circular aperture of $0''.5$ radius (background estimated in a $0''.6$ – $0''.8$ annulus).

Finally, reduced and calibrated images were retrieved from the *HST* scientific archive, acquired with the filters F210M (FOC; $\lambda = 2179.4 \text{ \AA}$, $\Delta\lambda = 381.5 \text{ \AA}$) and F606W (WFPC2; $\lambda = 6001.3 \text{ \AA}$, $\Delta\lambda = 1498.8 \text{ \AA}$). This corresponds to the same *HST* dataset as presented in González Delgado et al. (1998). The photometry in the *HST* images was extracted using a circular

aperture of $0''.14$ radius, subtracting the background estimated in a $0''.2$ – $0''.3$ annulus (see Table 1).

3. Results

3.1. Morphology

As probed by the *HST*/FOC image (González Delgado et al. 1998), the nucleus of IC 3639 is an extended UV source, with a size of $0''.8 \times 0''.4$ ($192 \times 96 \text{ pc}^2$). The nuclear emission is resolved into a substructure formed by three distinct regions: a central core likely associated with the AGN and two side lobes associated with star formation (see Fig. 1). In the *L*, *M*, and *N*-bands, the morphology shows only a point-like source at an angular resolution of $< 0''.4$ (see fig. 3 in Gandhi et al. 2009). This means that the UV side lobes do not show any counterpart in the mid-IR images (see Fig. 1). Although Asmus et al. (2014) classify IC 3639 as a marginally resolved source in the mid-IR NEII_2 narrow-band filter image ($\text{FWHM} \sim 0''.39 \sim 91 \text{ pc}$, $PA \sim 79^\circ$), such extension is not detected in any of the other filters. Consequently, Asmus et al. (2016) classify the source as non-extended ($\text{FWHM} \leq 0''.34 \sim 80 \text{ pc}$). Hereafter we will adopt 80 pc as a conservative upper limit to the size of the source, although the point-like morphology of this nucleus in VISIR images suggests a narrower flux distribution with $\text{FWHM} \leq 50 \text{ pc}$ as a more plausible scenario. The two UV lobes are brighter than the nucleus in the F210M filter, but they become fainter at longer wavelengths in the F606W filter. Thus, the bright point-like mid-IR source is assumed to be the counterpart of the central UV/optical peak. The origin of the central optical peak is not clear, since IC 3639 is a type 2 Compton-thick nucleus (Guainazzi et al. 2005) and thus the AGN should be covered by the obscuring torus in this range. Alternatively, the UV/optical emission might be associated with star-formation or the narrow-line region (NLR).

3.2. The mid-IR spectrum

Fig. 2 shows the mid-IR spectra of IC 3639 obtained with VLT/VISIR (in red) and *Spitzer*/IRS (in light and dark green for

the full-aperture and optimal-difference spectra, respectively). Three main aspects emerge from the analysis of these data: *i*) the continuum emission is consistent for both instruments, in terms of flux and spectral slope, in agreement with a point-like source dominating the total mid-IR flux in the inner kpc of the galaxy; *ii*) the presence of strong fine-structure emission lines corresponding to both low- (e.g. [Ne II], [S IV]) and high-ionisation species (e.g. [Ne V], [O IV]). About 74% of the [Ne II]_{12.8 μm} line flux seen in the full-aperture extraction from *Spitzer*/IRS is still present in the smaller slit aperture of the VISIR spectrum (see Table 1), suggesting that the low-ionisation gas is mostly unresolved at a resolution of ~ 80 pc; *iii*) the intense polycyclic aromatic hydrocarbon (PAH) feature at 11.3 μm detected in the full-aperture IRS spectrum becomes a factor of ~ 3 fainter in both the VISIR and the optimal-difference IRS spectra (the features at 6.2, 7.7, 8.6, and 17 μm are also detected with IRS in the low-spectral resolution mode; see Wu et al. 2009, Diamond-Stanic & Rieke 2010, LaMassa et al. 2012). Most of the PAH_{11.3 μm} emission and a fraction of the [Ne II]_{12.8 μm} line flux seem to come from diffuse emission extended over an area of $4''.7 \times 11''.3$, and thus are removed in the optimal-difference IRS spectrum.

For comparison, Fig. 2 also shows the photometry derived from the VISIR NEII acquisition image, plus additional sub-arcsec aperture measurements in the literature (black dots, see Table 1; Gandhi et al. 2009; Asmus et al. 2014). Error bars in the horizontal and vertical axes correspond to filter FWHM bandwidths and flux uncertainties, respectively. For a better comparison with the imaging data, synthetic photometry was also performed on the VISIR spectrum (black squares in Fig. 2), using the *pysynphot* package included in STSCI_PYTHON⁵ and the transmission curves for: the VISIR filters⁶ PAH2 (11.3 μm, $\Delta\lambda 0.59$ μm), NEII (12.81 μm, $\Delta\lambda 0.21$ μm), NEII_2 (13.04 μm, $\Delta\lambda 0.22$ μm); and the T-ReCS *N*-band filter (10.36 μm, $\Delta\lambda 2.64$ μm). Fluxes derived from imaging photometry are in agreement, within uncertainties, with the spectrophotometric measurements. Thus, possible variability in the mid-IR is not detected for the dataset analysed here, which covers the period 2004–2012.

3.3. MIDI correlated flux distribution

The comparison between the single-dish and the interferometric measurements provides us with a first guess of the mid-IR brightness distribution. The VISIR total flux of ~ 320 mJy, coming from spatial scales of less than $0''.5$ (see Sect. 2), is much brighter than the MIDI correlated flux at short baselines (46 m, corresponding to a spatial scale of ~ 47 mas; blue square in Fig. 2), which drops to $F_\nu = 84 \pm 17$ mJy. That is a factor of 3–4 times fainter than the continuum level in the VISIR spectrum, suggesting that a large fraction of the mid-IR flux is extended on a spatial scale of a few tens of parsecs. In Fig. 3 we explore four different scenarios for the mid-IR brightness distribution to explain the MIDI correlated fluxes.

Scenario 1: a single component with a Gaussian brightness distribution, which is progressively resolved with increasing baseline (grey-solid line in Fig. 3). In this case, the best fit of the single-dish *N*-band measurements and the MIDI correlated fluxes yields a FWHM of 5.8 ± 0.3 pc, at the distance of IC 3639. To estimate the fit error we used a bootstrapping Monte-Carlo

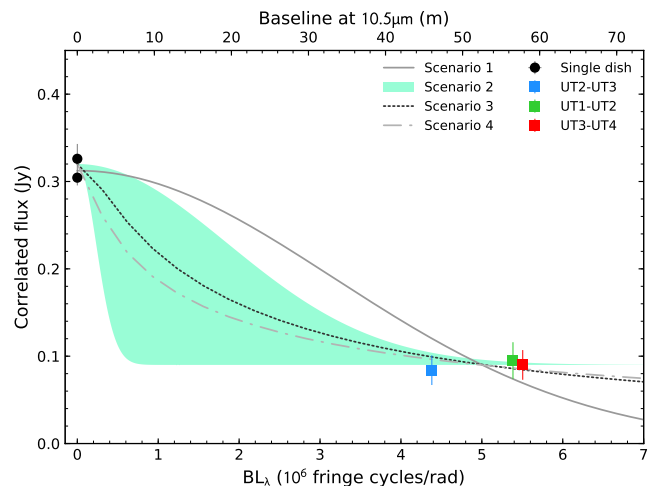


Fig. 3. Black dots represent the total flux measured by single dish telescopes (VISIR/PAH2 and T-ReCS/*N*-band), and filled squares represent the correlated fluxes measured by MIDI. Four possible scenarios are shown: a compact Gaussian distribution with $\text{FWHM} = 5.8 \pm 0.3$ pc in size (grey-solid line); an unresolved source plus a partially resolved Gaussian component of ~ 10 –80 pc (core-halo configuration; light green-shaded area); a power-law distribution with an inner radius of $R_{\text{in}} = 0.08$ pc, a half-light radius of $R_{1/2} = 1.8$ pc, an extended dust density distribution ($\alpha = 0.5$), and a temperature gradient index for ISM grains ($\beta = -0.36$; back-dotted line); a power-law distribution with an inner radius of $R_{\text{in}} = 0.4$ pc, $R_{1/2} = 7.3$ pc, a flat density distribution ($\alpha = 0$), and a temperature gradient index for ISM grains ($\beta = -0.36$; grey-dot-dashed line).

routine that generates a set of synthetic data from the observed values plus a normal distribution based on the observed errors. The final fit parameters and associated errors correspond, respectively, to the average and dispersion values obtained after fitting 1000 synthetic datasets.

Scenario 2: an unresolved point source plus a partially resolved Gaussian component with $\text{FWHM} \sim 10$ –80 pc (core-halo configuration; light green-shaded area). This scenario is motivated by the finding of such structures in several other AGN (c.f. Bartscher et al. 2013). The size of the extended component is constrained by the unresolved flux in single-dish observations ($\lesssim 80$ pc) and the flat visibility distribution seen by MIDI ($\gtrsim 10$ pc). Therefore, the unresolved component only accounts for $\sim 28\%$ of the total nuclear mid-IR flux, while 72% is radiated by an extended structure of a few tens of parsecs in size, unresolved by the single-dish observations but completely resolved by MIDI (Fig. 3). In contrast to the compact Gaussian configuration, this scenario explains the flat distribution of the correlated fluxes seen by MIDI.

Scenario 3: a single power-law distribution as described in Kishimoto et al. (2007, 2011). We assume an inner torus radius of $R_{\text{in}} = 0.08$ pc (from Suganuma et al. 2006; Kishimoto et al. 2007), corresponding to a nuclear UV luminosity of $L_{\text{UV}} \sim 3 \times 10^{44}$ erg s $^{-1}$, which was derived from the $L_X \sim 2 \times 10^{43}$ erg s $^{-1}$ based on *NuSTAR* observations (from Boorman et al. 2016, adapted to the distance used in this work) and the $L_{\text{UV}}-L_X$ relation from Marchese et al. (2012). We further assume a sublimation temperature of 1500 K, a grain size of 0.05 μm, and a dust temperature gradient index of $\beta = -0.36$, corresponding to ISM grains [$T \propto (r/R_{\text{in}})^\beta$; Barvainis 1987]. This scenario (black-dotted line in Fig. 3) could explain the visibilities by using a very extended dust density distribution [$\alpha = 0.5$, for $S_\nu \propto (r/R_{\text{in}})^\alpha$].

⁵ STSCI_PYTHON and PyRAF are products of the Space Telescope Science Institute, which is operated by AURA for NASA.

⁶ <http://www.eso.org/sci/facilities/paranal/instruments/visir/inst/>

This geometry implies a decreasing dust density with decreasing radius in order to reproduce the rapid drop in visibility with increasing baseline length, i.e. a torus with a lower concentration towards the centre.

Scenario 4: a single power-law distribution with $R_{\text{in}} = 0.4$ pc, which implies a $L_{\text{UV}} \sim 7 \times 10^{45} \text{ erg s}^{-1}$, and a flat dust density distribution ($\alpha = 0$). In this configuration the brightness radial gradient is determined only by the temperature gradient. This model is able to reproduce the observed visibilities using a flat density distribution (grey dot-dashed line in Fig. 3), but requires that little or no dust emission at all should come from the innermost ~ 0.4 pc. An inner radius of roughly half a parsec would imply a very high UV luminosity ($\sim 7 \times 10^{45} \text{ erg s}^{-1}$), which is significantly larger than the upper error limit of $L_{\text{disc}} < 1.3 \times 10^{45} \text{ erg s}^{-1}$ given by Boorman et al. (2016) at 90% confidence. The correlated flux predicted would overestimate the MIDI measurements if either a fainter luminosity is considered (corresponding to a smaller R_{in}), a more concentrated dust distribution is used ($\alpha < 0$), or a temperature gradient index for large grains ($\beta \sim -0.5$) is assumed.

In summary we conclude that from these four scenarios the core-halo configuration (scenario 2) seems to agree best to the observations. The power law distribution can also be accommodated to the observed visibilities, but a very large inner radius or a very extended dust density distribution should be used in order to balance the compact brightness distribution derived from the temperature gradient. As we will show in the following section, the core-halo scenario is in good agreement with the physical picture emerging when additional observational evidences are taken into account.

4. Discussion

The main questions that arise on the nature of the nuclear emission in IC 3639 are: *i*) the relative contribution of the AGN and the starburst to the mid-IR emission; and *ii*) the physical properties of these two components, i.e. their size, geometry, and spectral shape. Our approach is to infer the relative AGN and starburst contributions using IR diagnostics based on fine-structure emission lines, the continuum shape, and spectral features such as PAH and the silicate band at $9.7 \mu\text{m}$ (Section 4.1), and compare these results with the analysis of the correlated flux distribution and the size of the mid-IR components resolved by MIDI (Section 4.2). Finally, we also use the multiwavelength spectral energy distribution (SED) to shed light on the nature of the nuclear emission (Section 4.3).

4.1. IR spectral features and colours

The relative contributions from the AGN and the starburst to the gas photoionisation can be inferred from the IR fine-structure emission lines. Both the AGN and the starburst are able to produce strong lines of low-ionisation species –e.g. $[\text{Ne II}]_{12.8 \mu\text{m}}$ and $[\text{S IV}]_{10.5 \mu\text{m}}$ – however the AGN is the dominant or the only contribution to emission lines of high-ionisation species, like $[\text{Ne V}]_{14.3 \mu\text{m}}$ and $[\text{O IV}]_{25.9 \mu\text{m}}$. Thus, line ratios of high- to low-ionisation species provide a reliable estimate of the relative contribution of these two components (Sturm et al. 2002; Meléndez et al. 2008). From the mid-IR line fluxes measured by Tommasin et al. (2008) in the *Spitzer*/IRS-SH and LH spectra listed in Table 1, we obtain the line ratios of $[\text{O IV}]_{25.9}/[\text{Ne II}]_{12.8} = 0.47 \pm 0.01$ and $[\text{Ne V}]_{14.3}/[\text{Ne II}]_{12.8} = 0.25 \pm 0.01$ (see Table 2). These values are far from those obtained in AGN-dominated nuclei (with typical ratios of $[\text{O IV}]_{25.9}/[\text{Ne II}]_{12.8} \gtrsim 1.4$ and

$[\text{Ne V}]_{14.3}/[\text{Ne II}]_{12.8} \gtrsim 0.6$; Sturm et al. 2002), but similar to the ratios found in ULIRGs, usually associated with strong star formation (Armus et al. 2006, 2007). Following Sturm et al. (2002), a simple linear mixing model suggests an AGN contribution of $\sim 17\%$ from the $[\text{O IV}]_{25.9}/[\text{Ne II}]_{12.8}$ ratio and $\sim 23\%$ from the $[\text{Ne V}]_{14.3}/[\text{Ne II}]_{12.8}$ ratio, in agreement with the results obtained by Meléndez et al. (2008) for the case of IC 3639. This result is supported by photoionisation models for AGN with ionisation parameter values in the $-2.5 < \log U < -1.5$ range, which predict a $\sim 30\%$ AGN contribution for $[\text{Ne V}]_{14.3}/[\text{Ne II}]_{12.8} \sim 0.3$ (Abel & Satyapal 2008). Additional line ratios such as $[\text{O IV}]_{25.9}/([\text{Ne II}]_{12.8} + [\text{Ne III}]_{15.6})$ and $[\text{O IV}]_{25.9}/[\text{O III}]_{88}$ (listed in Table 2), which are more robust diagnostics for the relative AGN/starburst contribution under harder radiation fields (e.g. Lutz et al. 1998, Fernández-Ontiveros et al. 2016), also suggest a dominant contribution of the starburst component to the low-ionisation emission lines.

The line ratio diagnostics still apply if we use the $[\text{Ne II}]_{12.8 \mu\text{m}}$ line flux measured in the VISIR spectrum, which contains about 74% of the flux seen by *Spitzer*/IRS for the same emission line in a much wider aperture (see Table 1). In this case, the relative AGN contribution would increase to $\sim 23\%$ from the $[\text{O IV}]_{25.9}/[\text{Ne II}]_{12.8}$ ratio and $\sim 30\%$ from the $[\text{Ne V}]_{14.3}/[\text{Ne II}]_{12.8}$ ratio, assuming the same linear mixing model as before. We note that the IR fine-structure lines have not been corrected by extinction, however the detection of $[\text{Ne V}]_{3426 \text{ Å}}$ emission in the optical spectrum (see fig. 9b in Storch-Bergmann et al. 1995) suggests that the NLR emission in this galaxy is not strongly affected by dust, thus the effect of extinction in the mid- to far-IR range is expected to be negligible.

In order to further test the relative contribution of the starburst component, we used additional diagnostics based on IR spectral features (see Table 2) and the shape of the continuum emission measured for IC 3639. The mid-IR colour $W1 - W2 = 0.87$ (3.4 to $4.6 \mu\text{m}$), taken from the Wide-field Infrared Survey Explorer (*WISE*) point-source catalogue, falls within the limit defined by Stern et al. (2012) for AGN-heated dust ($W1 - W2 > 0.8$, $W2 < 15$). However, the $W2 - W3 = 4.27$ (4.6 to $11.6 \mu\text{m}$) and $W3 - W4 = 3.10$ (11.6 to $22.1 \mu\text{m}$) values place IC 3639 outside of the colour wedge defined by Mateos et al. (2012) for luminous AGN, and rather close to the mid-IR colours of M82 or Arp 220. A more detailed analysis of the continuum emission for IC 3639 has been performed recently by Gruppioni et al. (2016), using a broad-band UV to far-IR SED decomposition technique. The latter combines spectral templates of the dusty torus, the accretion disc, and various stellar populations (see Berta et al. 2013 for further details). These authors find an AGN fraction of $\sim 0.3 \pm 0.6$ for the nucleus in the $5\text{--}40 \mu\text{m}$ range, in agreement with our results albeit with very large uncertainty.

Finally, we analyse other IR spectral features such as the PAH and silicate bands. In this regard, the equivalent width of the PAH complex at $6.2 \mu\text{m}$ is consistent with a mixed contribution of both AGN and star formation (Petric et al. 2011). A further analysis comparing the ratios of the $\text{PAH}_{6.2 \mu\text{m}}$ flux to the $5.3\text{--}5.8 \mu\text{m}$ continuum and the continuum ratio between $14\text{--}16 \mu\text{m}$ and $5.3\text{--}5.8 \mu\text{m}$ (following Laurent et al. 2000, Armus et al. 2007, and Veilleux et al. 2009; values listed in Table 2), suggests that the heating of both PAH and dust grains is consistent with a combination of $\sim 50\%$ AGN and a mixture of emission from H II and photo-dissociation regions (PDR) for the remaining half fraction. This is also in agreement with the relatively high degree of PAH excitation inferred from the PAH ratios $F_{6.2 \mu\text{m}}/F_{7.7 \mu\text{m}}$ vs. $F_{11.3 \mu\text{m}}/F_{7.7 \mu\text{m}}$ (Stierwalt et al. 2014). We note that the diagnostics based on PAH features, specially those using the IRS-

Table 2. Mid-IR spectral lines and diagnostics measured for IC 3639 including: line ratios, equivalent width (EW) of diverse PAH features, flux ratios of different PAH complexes, strength of the silicate absorption band at 9.7 μm (S_{sil}), and PAH-to-integrated continuum ratios.

Line/Diagnostic	Value	Ref.
[Ne v] _{14.3} /[Ne II] _{12.8}	0.25 ± 0.01	Tommasin et al. (2008)
	0.33 ± 0.02^a	This Work
[O IV] _{25.9} /[Ne II] _{12.8}	0.47 ± 0.01	Tommasin et al. (2008)
	0.63 ± 0.03^a	This Work
[O IV] _{25.9} /([Ne II] _{12.8} + [Ne III] _{15.6})	0.29 ± 0.01	Fernández-Ontiveros et al. (2016)
[O IV] _{25.9} /[O III] ₈₈	0.51 ± 0.02	Fernández-Ontiveros et al. (2016)
EW(PAH _{6.2 μm})	$0.185 \pm 0.003 \mu\text{m}$	Wu et al. (2009)
EW(PAH _{7.7 μm})	$1.39 \mu\text{m}$	LaMassa et al. (2012)
EW(PAH _{11.3 μm})	$0.39 \mu\text{m}$	LaMassa et al. (2012)
EW(PAH _{17 μm})	$0.13 \mu\text{m}$	LaMassa et al. (2012)
$f_{\text{PAH}6.2 \mu\text{m}}$	0.14	Wu et al. (2009), LaMassa et al. (2012)
$f_{\text{PAH}7.7 \mu\text{m}}$		
$f_{\text{PAH}11.3 \mu\text{m}}$	0.29	LaMassa et al. (2012)
$f_{\text{PAH}17 \mu\text{m}}$		
S_{sil}	-0.312	Wu et al. (2009)
$\log \left(\frac{f_{\text{PAH}6.2 \mu\text{m}}}{f_{5.3-5.8 \mu\text{m}}} \right)$	~ 0.007	This Work
$\log \left(\frac{f_{14-16 \mu\text{m}}}{f_{5.3-5.8 \mu\text{m}}} \right)$	~ 1.05	This Work

Notes. ^(a) Using the [Ne II]_{12.8 μm} flux measured in the VISIR spectrum.

SL low-resolution spectra (slit width of $3''6 \times 57''$), are probably dominated by the extended emission with little contribution from the nuclear unresolved source, as shown by the comparison between the full-aperture and the optimal-difference IRS-HR spectra (light green and dark green lines in Fig. 2, respectively). Finally, the EW(PAH_{6.2 μm}) was compared to the strength of the 9.7 μm silicate feature, S_{sil} , following the diagnostics in Spoon et al. (2007). The latter places IC 3639 in the intermediate region between galaxies with a mid-IR spectrum dominated by AGN-heated dust and PAH-dominated spectra typical of starburst galaxies, with EW(PAH_{6.2 μm}) and S_{sil} similar to other Seyfert nuclei in LIRGs with a strong contribution from star formation, such as NGC 7469 (Genzel et al. 1995).

4.2. A compact AGN/starburst nucleus?

For a mid-IR luminosity of a few times $10^{42} \text{ erg s}^{-1}$, the expected size distribution of the torus is about 1 pc, based on interferometric observations of nearby AGN (Tristram et al. 2009; Tristram & Schartmann 2011; Bartscher et al. 2013). This is in agreement with the core-halo configuration shown in Fig. 3, in which the AGN dominates the unresolved emission seen by MIDI. Extended nuclear emission in the mid-IR has been detected for other nearby AGN, for instance, an extended component with a size of $\sim 200 \text{ pc}$ and a temperature of $\sim 165 \text{ K}$ was reported for the nucleus of NGC 4151 by Radomski et al. (2003). However, these authors conclude that the extended emission can be ascribed to dust grains in the NLR and not to the torus. This is in line with the detection of mid-IR emission extended along the axis direction of several AGN over scales of few tens to few hundreds of parsecs in size (also known as polar dust; Hönig et al. 2013, Asmus et al. 2016), but also at subparsec to few parsecs scales in mid-IR interferometric observations (e.g. Hönig et al. 2013, Tristram et al. 2014, López-Gonzaga et al. 2014). A framework to explain these observations has been proposed recently by Hönig & Kishimoto (2017), where the torus is modelled as a compact disc plus an dusty wind blown by the active nucleus along the axis of the system. In the case of IC 3639, the extended

dusty wind could possibly explain the extended component resolved by MIDI in the mid-IR. However, in order to reconcile this scenario with the measured line ratios, a considerable contribution from star formation should occur somewhere within the disc-plus-wind structure. Alternatively, an uncommon weak ionisation radiation field from the AGN with an ionisation parameter of $\log U \lesssim -3$ would have to be invoked in order to reproduce a [Ne v]_{14.3}/[Ne II]_{12.8} ratio of ~ 0.3 without additional contribution from star formation activity to the photoionised gas (Abel & Satyapal 2008). Finally, the three correlated fluxes measured by MIDI along different baseline orientations (see right panel in Fig. 1) are consistent, thus there is no evidence for a possible extension along a preferential direction.

The radial mid-IR brightness distribution seen by MIDI is flat between 46 and 58 m. Thus, a single Gaussian component does not provide a good fit to the visibilities, as shown in Fig. 3. A single power-law distribution can reproduce the estimated visibilities, but only after imposing restrictions on the geometry: either the dust density profile decreases steeply towards the AGN with decreasing radius [$\propto (r/R_{\text{in}})^{0.5}$; dotted-black line in Fig. 3], in contrast with other AGN observed with mid-IR interferometry ($\alpha \lesssim 0$, Kishimoto et al. 2011); or the inner radius is significantly larger as expected from the AGN luminosity for this galaxy ($\gtrsim 0.4 \text{ pc}$; dot-dashed grey line). Both scenarios imply a lower concentration of dust in the innermost region around the AGN to balance for the steep brightness profile imposed by the temperature gradient ($\beta = -0.36$ for ISM dust). If the temperature distribution is steeper when compared to ISM grains (e.g. $\beta = -0.5$ for large grains), an even less concentrated dust distribution (larger α and/or R_{in}) would be required to fit the visibilities measured by MIDI. Therefore, none of these alternatives seem to be an appealing scenario to describe the mid-IR brightness distribution in IC 3639.

We favour the core-halo configuration (scenario 2), represented in Fig. 3 by an extended Gaussian (10–80 pc) plus an unresolved source (light green-shaded area). The extended component dominates the total mid-IR emission (72%) and would be associated to dust heated by star formation, while the unre-

solved component (28% of the total mid-IR flux) is associated to the AGN. This result is in good agreement with diagnostics based on IR fine-structure lines: the strength of low-excitation lines, such as $[\text{Ne II}]_{12.8\mu\text{m}}$, compared to high-excitation transitions ($[\text{Ne V}]_{14.3\mu\text{m}}$, $[\text{O IV}]_{25.9\mu\text{m}}$) suggests that star formation contributes about 67–70% to the gas ionisation, with a remaining 23–30% due to AGN activity (Section 4.1). Furthermore, similar values for the relative AGN/starburst contributions are derived from the decomposition of the mid-IR continuum, as shown by Gruppioni et al. (2016). For these reasons we favour the extended core-halo configuration shown in Fig. 3 as the most consistent explanation for the characteristics of the brightness distribution, the ionised gas, and the shape of the IR continuum emission in IC 3639. In this scenario, the unresolved component ($\sim 30\%$ of the flux) corresponds to the AGN heated dust in the innermost few parsecs ($\lesssim 10$ pc), while most of the IR emission (70%) is associated to dust heated by the starburst component, extended over a spatial scale of ~ 10 –80 pc.

However, the case of IC 3639 is remarkable due to the compactness of the whole system: a strong starburst and an active nucleus coexist in the central 80 pc of the galaxy. This scenario is consistent with a nuclear SFR of $\sim 0.26 M_{\odot} \text{ yr}^{-1}$ derived from the VISIR PAH $_{11.3\mu\text{m}}$ flux in Table 1 and the linear fit calibration given by Shipley et al. (2016), although it is in contrast with the much lower value of $\sim 5 \times 10^{-3} M_{\odot} \text{ yr}^{-1}$ estimated from the UV luminosity in the filter F210M (from Table 1 and the NUV calibration in Kennicutt & Evans 2012). Thus, a large fraction of the SFR might be obscured in the optical/UV range. LaMassa et al. (2017) suggest that a strong starburst contribution might have an important role to explain the large equivalent width of the Fe K α X-ray line. Therefore the starburst component could be responsible for a significant part of the obscuration of the AGN, supporting also the geometrical thickness of the torus structure through stellar winds and SNe explosions (Wada & Norman 2002, Vollmer et al. 2008, Schartmann et al. 2009, Armour & Ballantyne 2012). The star formation activity could be feeding a moderate BH ($7.3 \times 10^6 M_{\odot}$; Wang & Zhang 2007), growing at a rate of $\log(L_{\text{bol}}/L_{\text{edd}}) \sim -1$ ($L_{\text{bol}} \sim 8 \times 10^{43} \text{ erg s}^{-1}$ derived from the flux measured with MIDI at $\sim 10 \mu\text{m}$ and the $L_{12\mu\text{m}}-L_{\text{bol}}$ relation from Spinoglio et al. 1995 for Seyfert galaxies in the 12 micron sample). IC 3639 is one of the most compact nuclear starbursts embedded in dust and surrounding an AGN, comparable to the case of NGC 4418. The latter has a brighter IR core ($L_{\text{bol}} \sim 4 \times 10^{44} \text{ erg s}^{-1}$) comparable in size ($\lesssim 20$ pc; Sakamoto et al. 2013, Costagliola et al. 2013), although affected by a much heavier obscuration in the mid-IR range ($S_{\text{sil}} \sim -4$; Spoon et al. 2001, Spoon et al. 2007).

4.3. Spectral energy distribution

The analysis of the SED gives us information on the mechanisms that produce the observed emission in the nucleus of IC 3639. A multiwavelength SED with subarcsec resolution (black dots in Fig. 4) is built using the flux measurements given in Table 1 plus comparable high-spatial resolution data in radio and X-ray wavelengths compiled from the literature (Sadler et al. 1995; Roy et al. 1994; Thean et al. 2000; Guainazzi et al. 2005). A low-spatial resolution SED based on measurements with larger apertures –several arcsecs to few arcmin– was also compiled (grey spikes), including measurements from NED⁷ as well as the *Her-*

schel/SPIRE (Pereira-Santaella et al. 2013), *Akari* (Yamauchi et al. 2011) and *WISE* point source catalogues. In all cases, UV, optical, and IR fluxes are corrected from Galactic extinction for a reddening of $E(B-V) = 0.06$ mag (Schlafly & Finkbeiner 2011), using the extinction law from Cardelli et al. (1989). For clarity, broad-band measurements including PAH features are not included in the low-spatial resolution SED. When compared with subarcsec resolution measurements, the low-spatial resolution SED reveals those spectral ranges dominated by the host galaxy (e.g. optical, radio) from those dominated by the nuclear/circumnuclear emission (mid-IR).

In this context, the interferometric data provide a key point to interpret the origin of the nuclear emission in IC 3639. About 70% of the mid-IR flux detected by VISIR originates in a scale of $\gtrsim 10$ –80 pc, and its continuum emission traced by the *Spitzer*/IRS spectrum peaks at 20–40 μm (see Fig. 4). For the case of thermal emission, the latter would correspond to a temperature value in the 70–150 K range. ISAAC measurements suggest the presence of hotter dust (~ 320 K) in the nuclear region. This range could be dominated by the AGN emission, but future *L*- and *M*-band interferometric observations with MATISSE (Multi AperTure mid-Infrared SpectroScopic Experiment) would be needed in order to probe this scenario. The shape of the SED shows a steep decline with increasing frequency (see Fig. 4), but it is not clear whether the UV/optical continuum is originated in the AGN itself or by a young starburst plus an underlying old stellar population as suggested by González Delgado et al. (1998). In this case the UV luminosity of the core represents only $\sim 1\%$ of the total luminosity reprocessed in the mid-IR range. This is in agreement with the Balmer decrement measured in IC 3639 ($H\alpha/H\beta = 6.1$), which corresponds to an extinction value of $A_V \sim 2.2$ mag, enough to reconcile the absorption-corrected UV luminosity ($L_{\text{UV}} \sim 8 \times 10^{43} \text{ erg s}^{-1}$) with the total mid-IR luminosity.

Alternatively, the nuclear UV emission and the extended lobes in Fig. 1 might be produced by the NLR and/or scattered light from the nucleus. This would be in agreement with the extended emission in the soft X-rays seen along the East–West direction by Ghosh et al. (2007). In order to avoid confusion, we use a different symbol for the nuclear UV/optical flux measurements in Fig. 4 (violet triangles).

5. Summary

In this work we combined interferometric observations at milliarcsec resolution in the mid-IR with a multi-wavelength dataset at subarcsec resolution. This approach allowed us to probe the physical scales associated with the nuclear emission in IC 3639. This Seyfert 2 galaxy shows a strong point-like source at the resolution of VISIR (~ 320 mJy within $\lesssim 340$ mas), but surprisingly most of the emission is spatially resolved in the MIDI data, showing correlated fluxes of only ~ 90 mJy, that is a factor 3 to 4 times lower when compared to the single dish measurements.

In order to explain this large drop in visibilities, we use a core-halo model with two components: an extended one with a few tens of parsecs in size (40–340 mas, ~ 10 –80 pc), and an unresolved core which accounts for the correlated fluxes measured by MIDI, i.e. $\sim 30\%$ of the total flux. A single dust component with a power law distribution could reproduce the observed visibilities, but a very extended dust distribution ($\alpha \gtrsim 0.4$ and/or $R_{\text{in}} \gtrsim 0.4$ pc), uncommon among other AGN observed with mid-IR interferometry, should be assumed. Alternatively, the presence of polar dust extended along the axis of the system could possibly explain the mid-IR brightness distribution in IC 3639.

⁷ The NASA/IPAC Extragalactic Database (NED) is operated by the Jet Propulsion Laboratory, California Institute of Technology, under contract with the National Aeronautics and Space Administration.

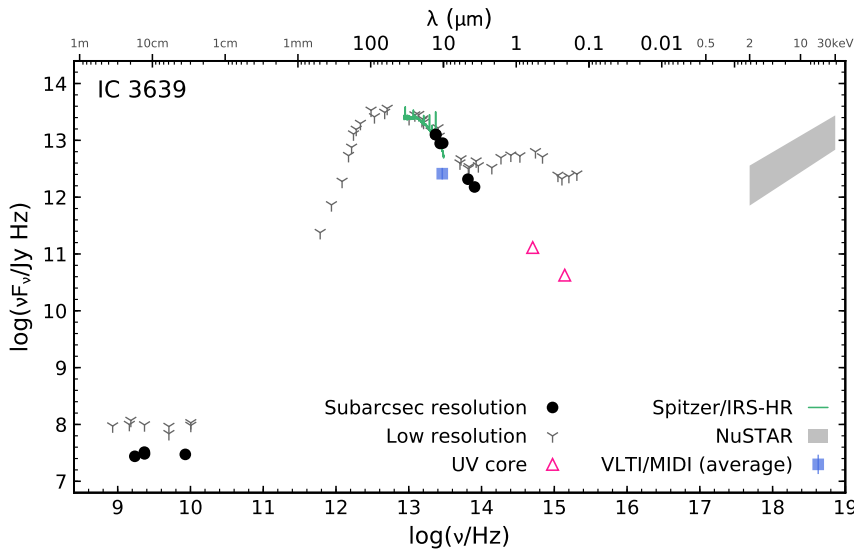


Fig. 4. SED for the nucleus of IC 3639 at a $\lesssim 0''.4$ resolution (black dots), compared with the MIDI measurement (blue square) and the *Spitzer*/IRS-HR optimal-difference spectrum from the CASSIS atlas (dark green line). Grey spikes represent the low-spatial resolution measurements, i.e. the integrated SED of the host galaxy. Violet triangles correspond to the UV core. The grey-shaded area indicates the 2–10 keV and 0.5–30 keV intrinsic fluxes estimated for the models T and M in Boorman et al. (2016).

From our study we conclude that the extended nuclear mid-IR component resolved by MIDI (~ 10 – 80 pc) is not likely associated with the AGN for the following reasons: *i*) its size is too large for a torus as discussed in Sect. 3.3; *ii*) several line ratios such as $[\text{Ne V}]_{14.3}/[\text{Ne II}]_{12.8}$, $[\text{O IV}]_{25.9}/[\text{Ne II}]_{12.8}$, $[\text{O IV}]_{25.9}/[\text{O III}]_{88}$, and $[\text{O IV}]_{25.9}/([\text{Ne II}]_{12.8} + [\text{Ne III}]_{15.6})$ suggest an AGN-starburst composite nucleus dominated by the starburst component; *iii*) the relative AGN-starburst contribution of ~ 30 – 70% , inferred from the mid-IR brightness distribution in the core-halo scenario, is in very good agreement with the relative contribution of the AGN-starburst components inferred from the ionisation of the IR fine-structure lines, and the shape of the IR continuum (Section 4.1).

Therefore, we favour the core-halo scenario as the most consistent explanation to describe the observed properties of the mid-IR nucleus in IC 3639. The total mid-IR emission is dominated by an extended component ascribed to star formation within the innermost 80 pc. The presence of an AGN is needed in order to explain the hard X-ray emission, the high-ionisation fine-structure lines in the spectrum, and the unresolved component detected by the MIDI interferometric observations. Furthermore, the proposed scenario for this galaxy could in fact be relatively common in other Seyfert galaxies. A large number of type 2 nuclei show strong point-like emission in the mid-IR at subarcsec scales, and this is commonly assumed to be the emission from the torus. Only the high-spatial resolution achieved with VLT/MIDI, combined with the multi-wavelength analysis at subarcsec scales, allowed us to disentangle the emission components in nucleus of IC 3639. Our results also highlight the difficulty when trying to separate the emission components or determine torus covering fractions from larger aperture SEDs as obtained with space telescopes. The next generation of interferometric instruments such as MATISSE at VLT, would be of great help to disentangle the different contributions to the mid-IR flux in the innermost parsecs of nearby AGN.

Acknowledgements. This research made use of Astropy, a community-developed core Python package for Astronomy (Astropy Collaboration, 2013). This research has made use of the NASA/IPAC Infrared Science Archive, which is operated by the Jet Propulsion Laboratory, California Institute of Technology, under contract with the National Aeronautics and Space Administration. J.A.F.O. acknowledges financial support from the Spanish Ministry of Economy and Competitiveness (MINECO) under grant number MEC-AYA2015-53753-P.

References

- Aalto, S., Muller, S., Costagliola, F., et al. 2017, ArXiv e-prints [arXiv:1702.05458]
 Abel, N. P. & Satyapal, S. 2008, ApJ, 678, 686
 Armour, J. N. & Ballantyne, D. R. 2012, ApJ, 752, 87
 Armus, L., Bernard-Salas, J., Spoon, H. W. W., et al. 2006, ApJ, 640, 204
 Armus, L., Charmandaris, V., Bernard-Salas, J., et al. 2007, ApJ, 656, 148
 Asmus, D., Höning, S. F., & Gandhi, P. 2016, ApJ, 822, 109
 Asmus, D., Höning, S. F., Gandhi, P., Smette, A., & Duschl, W. J. 2014, MNRAS, 439, 1648
 Barvainis, R. 1987, ApJ, 320, 537
 Bassani, L., Dadina, M., Maiolino, R., et al. 1999, ApJS, 121, 473
 Berta, S., Lutz, D., Santini, P., et al. 2013, A&A, 551, A100
 Boorman, P. G., Gandhi, P., Alexander, D. M., et al. 2016, ApJ, 833, 245
 Burtscher, L., Meisenheimer, K., Tristram, K. R. W., et al. 2013, A&A, 558, A149
 Burtscher, L., Tristram, K. R. W., Jaffe, W. J., & Meisenheimer, K. 2012, in Society of Photo-Optical Instrumentation Engineers (SPIE) Conference Series, Vol. 8445, Society of Photo-Optical Instrumentation Engineers (SPIE) Conference Series
 Cardelli, J. A., Clayton, G. C., & Mathis, J. S. 1989, ApJ, 345, 245
 Ciotti, L. & Ostriker, J. P. 2007, ApJ, 665, 1038
 Costagliola, F., Aalto, S., Sakamoto, K., et al. 2013, A&A, 556, A66
 Davies, R. I., Müller Sánchez, F., Genzel, R., et al. 2007, ApJ, 671, 1388
 Devillard, N. 1999, in Astronomical Society of the Pacific Conference Series, Vol. 172, Astronomical Data Analysis Software and Systems VIII, ed. D. M. Mehringer, R. L. Plante, & D. A. Roberts, 333
 Di Matteo, T., Springel, V., & Hernquist, L. 2005, Nature, 433, 604
 Diamond-Stanic, A. M. & Rieke, G. H. 2010, ApJ, 724, 140
 Esquej, P., Alonso-Herrero, A., González-Martín, O., et al. 2014, ApJ, 780, 86
 Fernández-Ontiveros, J. A., Spinoglio, L., Pereira-Santaella, M., et al. 2016, ApJS, 226, 19
 Fischer, T. C., Crenshaw, D. M., Kraemer, S. B., & Schmitt, H. R. 2013, ApJS, 209, 1
 Gallimore, J. F., Elitzur, M., Maiolino, R., et al. 2016, ApJ, 829, L7
 Gandhi, P., Horst, H., Smette, A., et al. 2009, A&A, 502, 457
 García-Burillo, S., Combes, F., Ramos Almeida, C., et al. 2016, ApJ, 823, L12
 Gebhardt, K., Bender, R., Bower, G., et al. 2000, ApJ, 539, L13
 Genzel, R., Weitzel, L., Tacconi-Garman, A. L. E., et al. 1995, ApJ, 444, 129
 Ghosh, H., Pogge, R. W., Mathur, S., Martini, P., & Shields, J. C. 2007, ApJ, 656, 105
 González Delgado, R. M., Heckman, T., Leitherer, C., et al. 1998, ApJ, 505, 174
 Gruppioni, C., Berta, S., Spinoglio, L., et al. 2016, MNRAS, 458, 4297
 Guainazzi, M., Matt, G., & Perola, G. C. 2005, A&A, 444, 119
 Heisler, C. A., Lumsden, S. L., & Bailey, J. A. 1997, Nature, 385, 700
 Höning, S. F. & Kishimoto, M. 2017, ApJ, 838, L20
 Höning, S. F., Kishimoto, M., Gandhi, P., et al. 2010, A&A, 515, A23
 Höning, S. F., Kishimoto, M., Tristram, K. R. W., et al. 2013, ApJ, 771, 87
 Jaffe, W., Meisenheimer, K., Röttgering, H. J. A., et al. 2004, Nature, 429, 47
 Jaffe, W. J. 2004, in Society of Photo-Optical Instrumentation Engineers (SPIE) Conference Series, Vol. 5491, Society of Photo-Optical Instrumentation Engineers (SPIE) Conference Series, ed. W. A. Traub, 715
 Kawakatu, N. & Wada, K. 2008, ApJ, 681, 73

- Kennicutt, R. C. & Evans, N. J. 2012, *ARA&A*, 50, 531
- Kishimoto, M., Hönig, S. F., Antonucci, R., et al. 2011, *A&A*, 536, A78
- Kishimoto, M., Hönig, S. F., Beckert, T., & Weigelt, G. 2007, *A&A*, 476, 713
- Knapen, J. H. 2005, *A&A*, 429, 141
- Kormendy, J. & Richstone, D. 1995, *ARA&A*, 33, 581
- Lagage, P. O., Pel, J. W., Authier, M., et al. 2004, *The Messenger*, 117, 12
- LaMassa, S. M., Heckman, T. M., Ptak, A., et al. 2012, *ApJ*, 758, 1
- LaMassa, S. M., Yaqoob, T., Levenson, N. A., et al. 2017, *ApJ*, 835, 91
- Laurent, O., Mirabel, I. F., Charmandaris, V., et al. 2000, *A&A*, 359, 887
- Lebouteiller, V., Barry, D. J., Goes, C., et al. 2015, *ApJS*, 218, 21
- Leggett, S. K., Hawarden, T. G., Currie, M. J., et al. 2003, *MNRAS*, 345, 144
- Leinert, C., Graser, U., Przygodda, F., et al. 2003, *Ap&SS*, 286, 73
- López-Gonzaga, N., Jaffe, W., Burtscher, L., Tristram, K. R. W., & Meisenheimer, K. 2014, *A&A*, 565, A71
- Lumsden, S. L., Heisler, C. A., Bailey, J. A., Hough, J. H., & Young, S. 2001, *MNRAS*, 327, 459
- Lutz, D., Kunze, D., Spoon, H. W. W., & Thornley, M. D. 1998, *A&A*, 333, L75
- Madau, P. & Dickinson, M. 2014, *ARA&A*, 52, 415
- Marchese, E., Della Ceca, R., Caccianiga, A., et al. 2012, *A&A*, 539, A48
- Mateos, S., Alonso-Herrero, A., Carrera, F. J., et al. 2012, *MNRAS*, 426, 3271
- Meléndez, M., Kraemer, S. B., Schmitt, H. R., et al. 2008, *ApJ*, 689, 95
- Pereira-Santaella, M., Spinoglio, L., Busquet, G., et al. 2013, *ApJ*, 768, 55
- Petric, A. O., Armus, L., Howell, J., et al. 2011, *ApJ*, 730, 28
- Radomski, J. T., Piña, R. K., Packham, C., et al. 2003, *ApJ*, 587, 117
- Roy, A. L., Norris, R. P., Kesteven, M. J., Troup, E. R., & Reynolds, J. E. 1994, *ApJ*, 432, 496
- Sadler, E. M., Slee, O. B., Reynolds, J. E., & Roy, A. L. 1995, *MNRAS*, 276, 1373
- Sakamoto, K., Aalto, S., Costagliola, F., et al. 2013, *ApJ*, 764, 42
- Schartmann, M., Meisenheimer, K., Klahr, H., et al. 2009, *MNRAS*, 393, 759
- Schlafly, E. F. & Finkbeiner, D. P. 2011, *ApJ*, 737, 103
- Shipley, H. V., Papovich, C., Rieke, G. H., Brown, M. J. I., & Moustakas, J. 2016, *ApJ*, 818, 60
- Spinoglio, L., Malkan, M. A., Rush, B., Carrasco, L., & Recillas-Cruz, E. 1995, *ApJ*, 453, 616
- Spoon, H. W. W., Keane, J. V., Tielens, A. G. G. M., Lutz, D., & Moorwood, A. F. M. 2001, *A&A*, 365, L353
- Spoon, H. W. W., Marshall, J. A., Houck, J. R., et al. 2007, *ApJ*, 654, L49
- Springel, V. & Hernquist, L. 2003, *MNRAS*, 339, 289
- Stern, D., Assef, R. J., Benford, D. J., et al. 2012, *ApJ*, 753, 30
- Stierwalt, S., Armus, L., Charmandaris, V., et al. 2014, *ApJ*, 790, 124
- Storchi-Bergmann, T., Kinney, A. L., & Challis, P. 1995, *ApJS*, 98, 103
- Sturm, E., Lutz, D., Verma, A., et al. 2002, *A&A*, 393, 821
- Suganuma, M., Yoshii, Y., Kobayashi, Y., et al. 2006, *ApJ*, 639, 46
- Temporin, S., Ciroi, S., Rafanelli, P., et al. 2003, *ApJS*, 148, 353
- Thean, A., Pedlar, A., Kukula, M. J., Baum, S. A., & O'Dea, C. P. 2000, *MNRAS*, 314, 573
- Tommasin, S., Spinoglio, L., Malkan, M. A., et al. 2008, *ApJ*, 676, 836
- Tristram, K. R. W., Burtscher, L., Jaffe, W., et al. 2014, *A&A*, 563, A82
- Tristram, K. R. W., Raban, D., Meisenheimer, K., et al. 2009, *A&A*, 502, 67
- Tristram, K. R. W. & Schartmann, M. 2011, *A&A*, 531, A99
- Veilleux, S., Rupke, D. S. N., Kim, D.-C., et al. 2009, *ApJS*, 182, 628
- Vollmer, B., Beckert, T., & Davies, R. I. 2008, *A&A*, 491, 441
- Wada, K. & Norman, C. A. 2002, *ApJ*, 566, L21
- Wang, J.-M. & Zhang, E.-P. 2007, *ApJ*, 660, 1072
- Weigelt, G., Wittkowski, M., Balega, Y. Y., et al. 2004, *A&A*, 425, 77
- Wild, V., Heckman, T., & Charlot, S. 2010, *MNRAS*, 405, 933
- Wilson, A. S., Shopbell, P. L., Simpson, C., et al. 2000, *AJ*, 120, 1325
- Wu, Y., Charmandaris, V., Huang, J., Spinoglio, L., & Tommasin, S. 2009, *ApJ*, 701, 658
- Wutschik, S., Schleicher, D. R. G., & Palmer, T. S. 2013, *A&A*, 560, A34
- Yamauchi, C., Fujishima, S., Ikeda, N., et al. 2011, *PASP*, 123, 852